Results in Materials 29 (2026) 100837

Contents lists available at ScienceDirect

Results in Materials

journal homepage: www.sciencedirect.com/journal/results-in-materials

Validation of material-invariant mechanical models for triply periodic minimal surface structures

Henri Kammler [a,b,1,*], Jan Kube [a,1], Hendrik Traub [a,1], Christian Hühne [a,b]

[a] Technische Universität Braunschweig, Institute of Mechanics and Adaptronics, Langer Kamp 6, 38106 Braunschweig, Germany
[b] German Aerospace Center, Institute of Lightweight Systems, Lilienthalplatz 7, 38108 Braunschweig, Germany

ARTICLE INFO

Keywords:
Cellular structures
TPMS
Gyroid
Primitive
SLA
SLS
Material-invariant

ABSTRACT

Their dual functionality makes triply periodic minimal surface (TPMS) sheet networks an ideal candidate for permeable, load-bearing cellular structures. The present study investigates Gyroid and Primitive structures in quasi-static compression. Cubic polymeric TPMS specimens of 90 mm edge length with a relative density between 0.1 and 0.7 are manufactured additively by means of selective laser sintering and stereolithography. Aiming at material-invariant findings, the authors test solid specimens to normalize cellular properties with the printed solid's properties. The resulting relative stiffness, strength, and energy absorption are modeled as a function of relative density. Mechanical models are obtained from tests with sintered Nylon 11 specimens. The relative compressive properties of Gyroid and Primitive structures differ marginally. A linear function describes their material utilization in approximation. Additionally, this study identifies and quantifies the constraints that selective laser sintering and stereolithography impose on the manufacturability and mechanical performance of TPMS specimens, emphasizing their relevance to application-related research using industry-oriented methods. A comparison with previous studies confirms that experimentally obtained results align more closely with the findings of FE analysis as the influence of defects diminishes. The modeled relative modulus found in this study corresponds with the work of other authors on different base materials in overlapping relative density intervals and underlines the material-independent mechanical characteristics of TPMS structures.

1. Introduction

Laminar flow control is considered to have great potential for sustainable aviation by reducing an aircraft's viscous drag by up to 31 % [1]. The viscous drag reduction can be further split into 18 % drag reduction on the wing and 13 % drag reduction on the fuselage, making the wing a promising region for laminar flow technology. While natural laminar flow (NLF) successfully achieves laminar flow on low-swept, subsonic wings, active laminar flow control (LFC) through boundary layer suction on the whole wing surface poses significant manufacturing challenges and results in extreme system complexity. Less complex hybrid laminar flow control (HLFC) [2] systems apply boundary layer suction only on the leading edge of transport aircraft wings extended by limited NLF, achieving partial laminar flow on the wing. Traub et al. [3] consider in their extended hybrid laminar flow (*x*HLFC) concept a combination of active LFC and NLF. They develop suction panels to apply boundary layer suction along the leading edge and on the rear part of the wing to achieve a fully laminar boundary layer. Their integral design approach is desired for the suction panels to reduce system complexity, avoid hole blockage, and minimize stress peaks. A promising lightweight design solution is based on sandwich panels: Two thin skins, with the outer one perforated to allow boundary layer suction [4,5], are supported by a porous, cellular, yet robust core structure. Next to its load-bearing capabilities [6], the core also guides and controls the suction flow. For the design of the leading-edge suction panels with respect to their mechanical function, the bird strike is the critical loading case. This study, as a first step, investigates the Gyroid core structure under quasi-static compressive loading. Hereby, linear elastic, plastic, and energy absorption characteristics are examined.

As common core materials, such as honeycomb and foams, do not provide multidirectional internal channels to ensure sufficient airflow, triply periodic minimal surface (TPMS) structures have been investigated in recent studies [3,4,6]. The present study is concerned with the Schwarz Primitive (P) and the Schoen Gyroid (G) as illustrated in Fig. 1. A multitude of unit cells is arranged to form the core

* Correspondence to: Lilienthalplatz 7, 38108 Braunschweig, Germany.
E-mail addresses: henri.kammler@dlr.de (H. Kammler), jan.kube@tu-braunschweig.de (J. Kube), h.traub@tu-braunschweig.de (H. Traub), christian.huehne@dlr.de (C. Hühne).
[1] These authors contributed equally to this work.

https://doi.org/10.1016/j.rinma.2025.100837
Received 7 April 2025; Received in revised form 8 October 2025; Accepted 4 December 2025
Available online 5 December 2025

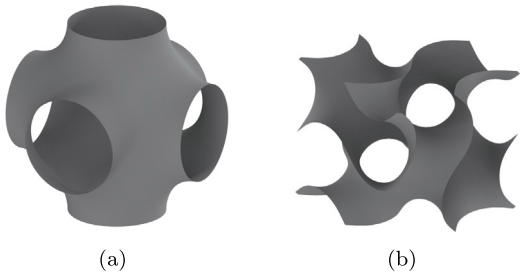

Fig. 1. TPMS unit cells: Schwarz Primitive (a) and Schoen Gyroid (b).

structure. Their open-cell geometry is advantageous for functionally integrated purposes as permeable load-bearing structures. Additive manufacturing concepts enable the geometrical design freedom required to manufacture suction panels as a single part.

Numerous studies have investigated the mechanical properties of TPMS structures [7–9]. However, these investigations often lack comparability due to variations in base materials, limited overlapping ranges of relative density, inconsistent definitions of mechanical properties, and non-standardized strain rates. Consequently, existing research does not provide an adequate foundation for designing suction panels with load-bearing functionality. Addressing this gap, the present study identifies and validates the compressive mechanical properties of Gyroid and Primitive sheet networks, ensuring applicability independent of base material and manufacturing method and enabling the reliable dimensioning of such structures.

1.1. TPMS structures under compressive load

Three parameters govern the mechanical properties of TPMS structures: The unit cell geometry, mechanical properties of the base material, and the relative density RD, which relates the cellular structure's density ρ^* to the base material's density ρ_s. When subjected to mechanical loads, TPMS structures exhibit non-uniform stress and strain distributions at the cellular level. However, describing the TPMS structure as a material of its own by using effective material properties is an appropriate approach for an entirety of multiple cells [10]. This approach allows for direct comparison with the solid base material properties, thereby assessing the performance of the cellular structure. Additionally, it can be used to engineer the wing integration of the previously described suction panels. By blurring localized stresses, this method substitutes complex TPMS structures and reduces overall design and computational costs.

Based on a generic cubic unit cell composed of cell edges and faces under compressive load F (Fig. 2) Gibson and Ashby [11] derive laws for the contribution of different cell deformation mechanisms to the total stiffness and strength of the cell and cellular structure scaling with RD. For the stiffness of closed cells in the linear-elastic regime, Gibson and Ashby find the contribution of cell-edge bending to scale with RD^2, the contribution of cell-face bending to scale with RD^3 and the contribution of cell-face stretching to scale with RD. This yields

$$\frac{E^*}{E_s} = C_1 \Phi^2 RD^2 + C_1' (1-\Phi) RD + C_1'' (1-\Phi)^3 RD^3 \tag{1}$$

for the effective compressive modulus of the cellular structure E^* relative to the compressive modulus of the solid base material E_s. The contribution of trapped gases inside the compressed cell is neglected for the porous geometries investigated in the present study. The parameter Φ describes how solid material is distributed between the edges and faces of cells, where $\Phi = 1$ indicates the absence of faces and $\Phi = 0$ signifies the absence of edges. The proportionality constants C_1 need to be determined empirically to adjust the scaling law for specific cell geometries.

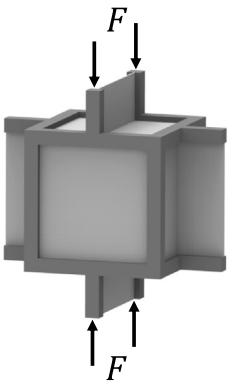

Fig. 2. Generic cubic closed unit cell under compressive load proposed by Gibson and Ashby [11].

Another approach to modeling the mechanical properties of cellular structures, often used in literature [7], involves using a power law with RD as the independent variable. For a given property of the base material P_s, the resulting effective property of the cellular structure P^* is

$$P^* = P_s \cdot \alpha \cdot RD^n . \tag{2}$$

The dimensionless proportionality factor α and the exponent n are determined empirically for a specific unit cell geometry and do not necessarily reflect a physical background. For stiffness and strength, $\alpha = n = 1$ gives the Voigt maximum limit [12]. It is achieved theoretically if the material of the cells is oriented along the load direction and free of imperfections and instability effects.

The design of unit cells for structural–mechanical applications aims to maximize the cellular structure's stiffness, strength, and energy absorption compared to the solid base material. Stability effects are to be minimized to increase material utilization μ (i.e., the maximum homogenized stress relative to the base material strength and relative density). Unlike strut-based cellular structures, junction-free TPMS sheet networks show minor stress concentrations when subjected to mechanical loads, increasing the structural efficiency [7]. Their self-supporting architecture reduces the sensitivity to instability effects, such as the buckling of cell components, and enables additive manufacturability without internal support structures. TPMS are characterized by a mean curvature equaling zero and connecting given boundaries by a single, non-self-intersecting surface, dividing space into two parts [13]. This surface is continued when concatenating multiple unit cells along all three dimensions. Cellular structures are obtained by thickening the TPMS, referred to as sheet networks, or by filling one of the two spaces with material, referred to as solid networks. For simplicity, the term *TPMS specimens* refers to sheet network specimens based on TPMS in the present study.

1.2. Previous studies on mechanics of TPMS structures

The mechanical properties of TPMS structures have been discussed in many previous studies. Al-Ketan and Abu Al-Rub [7] provide an overview of numerically and experimentally obtained results for numerous TPMS geometries, including data on Gyroid and Primitive structures developed as sheet and solid networks. Most studies investigate TPMS structures with a relative density below 0.5 and in a range of 10 to 20 percent points, constraining the validity of the obtained mechanical models. As opposed to the power law (eq. (2)), all mechanical models communicated in [7] are based on absolute coefficients $C = P_s \cdot \alpha$.

While Bobbert et al. [8] and Abueidda et al. [14] lack information on base material properties P_s, Al Ketan et al. [15] and Abou-Ali et al. [16] provide manufacturer's data that is only representative if determined using the same printing parameters. Zhang et al. [9] conduct tests on the printed solid base material for a load case different from the cellular specimens. However, the characterization of structural–mechanical behavior and comparability of different studies requires results independent of the base material and printing parameters. Dimensionless relative parameters P^*/P_s provide a valuable approach to modeling mechanical properties of cellular structures [6]. Given that P_s represents the theoretical upper limit of P^* for $RD \rightarrow 1$, the relative parameters predict the mechanical properties of the cellular structure while also reflecting the structural performance. Traub et al. [6] hypothesize the material-independent character of representative relative parameters P^*/P_s for respective TPMS structures. In practice, P_s is determined by conducting tests with solid specimens printed with the same parameters used for the cellular specimens [6]. Matching the 3D printing parameters is particularly important for normalization, as small deviations in the manufacturing process can lead to significant changes in mechanical properties, as shown by Bazyar et al. [17] for the SLA process.

Luo et al. [18] derive normalized power laws based on experimental and numerical analyses of Gyroid structures under compressive loads. Their printing parameters and base material properties P_s are consistent with the values reported by Jin et al. [19]. These base material properties were measured under tensile loads and may not represent the upper limit of the Gyroid's compressive properties P^* for $RD \rightarrow 1$. Song et al. [20] conduct compressive tests on interpenetrating phase composites with TPMS geometries and supplement their experiments by evaluating the compressive strength of the printed base material according to ASTM D695-11.

Various studies found in the literature use inconsistent definitions of mechanical properties. According to Table 3 in [7], many studies provide either yield or maximum strength. Often, it is not clear how these properties differ. According to ASTM D695-15 [21] for compressive properties of rigid plastics, the compressive strength can have no real meaning if a specimen is deformed under steadily rising compressive stress without any distinct failure. In accordance, ASTM D1621-16 [22] for compressive properties of rigid cellular plastics defines compressive strength as the stress at the yield point. Contrary to common practice, Abou-Ali et al. [23] define the compressive strength of TPMS specimens as "the maximum strength reached before densification." A strain of 60% is defined as densification, offering no further explanation. They calculate the plateau stress σ^*_{plat} of cellular specimens based on the assumed onset strain of densification. Without explanation or reflecting the relative densities investigated, σ^*_{plat} is defined as the average compressive stress between 20 % to 30 % [23], 20 % to 40 % [15] or 20 % to 50 % [16] compressive strain. Similar strain intervals determine the volume-specific energy absorption W^* by integrating over compressive strain: 0 % to 40 % [16], 0 % to 60 % [23], and 25 % to 60 % [14,24]. It should be noted that the upper boundary does not necessarily equal the assumed onset strain of densification. Zhang [9] and Song et al. [20], however, determine the onset strain of densification based on an energy efficiency parameter $\eta(\varepsilon)$ defined by Li et al. [25] providing consistent results for various relative densities (see Section 2.5).

Traub et al. [6] address the lack of comparability in the aforementioned studies. They conduct quasi-static compressive tests with Gyroid, Primitive, and honeycomb specimens made of Tough 2000 resin and normalize the compressive modulus and strength with experimentally determined base material properties. In addition, they analyze the mechanical behavior of the Gyroid geometry numerically for quasi-static compressive, shear, and hydro-static load. The relative compressive modulus and strength are modeled as a function of RD using the Gibson–Ashby-model (eq. (1)) and compared with the power law (eq. (2)). It is found that honeycombs outperform both TPMS geometries under compressive load in relative stiffness and strength. In contrast to honeycombs, the relative material properties of the Gyroid largely remain the same for shear and hydro-static loading. Both TPMS specimens exhibit an increasing material utilization from 8.9% at $RD = 16\%$ to 21.2% at $RD = 36\%$. The simulations, however, cannot be validated by the experiments as the measured relative properties are lower by a factor of two. Traub et al. assume that an extended experimental study, which covers a greater range of relative densities and includes at least two base materials, will enable the development and validation of a material-independent model for relative structural properties. The present study reacts to the research needs identified and focuses on the experimental investigation of the Gyroid and Primitive sheet structure under quasi-static compressive load. It aims to develop a material-independent model based on specimens made of Tough 2000 and validate it with specimens made of Nylon 11. As suggested by Traub et al. the edge length of the cubic specimens in the present study is larger than 40 mm to minimize the influence of manufacturing imperfections.

The specimens are manufactured using stereolithography and selective laser sintering. Quasi-static compressive tests provide effective compressive stress and strain values determining the cellular structures' relative properties. The Gibson–Ashby approach is used to model the relative properties as a function of the relative density and to compare the results with the work of other authors. It is found that Gyroid and Primitive sheet networks show similar compressive stiffness and strength characteristics and a material utilization that increases linearly with the relative density. The present study confirms the material-independent nature of both investigated TPMS geometries.

2. Experimental method

Designing the cellular specimens requires defining the cellular parameters, main dimensions, and the two base materials. The cellular and solid specimens are manufactured and post-processed according to their respective manufacturing methods. To assess the precision of the applied manufacturing methods, the actual relative density of the cellular specimens is measured and compared with the nominal value. To determine the compressive stress–strain curves, two calibrated universal test machines with different load cells are used for the quasi-static compressive tests. The effective material properties are calculated and normalized using representative base material properties.

2.1. Designing TPMS specimens

No standard for compressive test methods explicitly addresses cellular lattice structures. The standards ASTM D1621-16 [22] and DIN EN ISO 844:2021-07 [26] cover compressive properties of rigid cellular plastics, more particularly foams, but do not exclude cellular lattice structures. These standards are a guideline for the specimen's dimensioning and testing in the present study.

The cubic TPMS specimens are defined by their cellular parameters and main dimensions. Cellular parameters include the TPMS geometry, the relative density RD, and the number of unit cells along each dimension n_{uc} as independent variables. Depending on the main dimensions, the length of each unit cell l_{uc} and the sheet thickness (in the case of sheet networks) can be calculated. In this study, the cellular parameters and main dimensions are defined based on previous studies and constrained by the manufacturing process.

In an experimental approach, the mechanical properties of cellular structures should represent an infinite compound despite the specimens containing a finite number of unit cells. Abueidda et al. [14] numerically investigate the Primitive geometry with a relative density $RD = 0.04$. Their results suggest that specimens of $4x4x4$ unit cells approximate the infinite compound well. The present study aims at verifying these results by varying $n_{uc} = \{4, 6, 9\}$. Four values of relative density are investigated: $RD = \{0.1, 0.2, 0.4, 0.7\}$. These cover

a wide range while maintaining manufacturability and appropriate manufacturing costs. Multiple factors influence the design of the main dimensions: Specimens should be large enough to ensure the sheet thickness t is within a manufacturable range for large n_{uc} and low RD. Large main dimensions simplify removing remaining resin (SLA process) and unsintered powder (SLS). However, small main dimensions reduce manufacturing time and material cost. In accordance with ASTM D1621 [22], the specimen edge length is defined to be $90\,mm = const$. The CAD-based regression approach from [6] for the Gyroid and Primitive sheet networks is extended to cover the complete relative density range. It yields empirical formulas for the relative density RD as a function of the sheet thickness t and the length of each unit cell l_{uc}:

$$RD \approx a \cdot \left(\frac{t}{l_{uc}}\right) + b \cdot \left(\frac{t}{l_{uc}}\right)^3 \tag{3}$$

with $a = 3.0918$, $b = -4.1887$, $R^2 = 0.99999$ for the Gyroid, and $a = 2.3520$, $b = -2.0080$, $R^2 = 0.99999$ for the Primitive, respectively. Cylindrical solid specimens are designed according to ASTM D695 [21] to determine the compressive properties of the base material.

Due to their complexity, TPMS specimens are difficult to design using conventional CAD software. Implicit functions f_G and f_P approximate the minimal surfaces:

$$f_P = \cos X + \cos Y + \cos Z \tag{4}$$

$$f_G = \sin X \cos Y + \sin Y \cos Z + \sin Z \cos X \tag{5}$$

with $X = 2\pi \cdot x/l_x$, $Y = 2\pi \cdot y/l_y$, $Z = 2\pi \cdot z/l_z$ at the Cartesian coordinates x, y, z with l_x, l_y, l_z being the unit cell length [27]. Isosurfaces are extracted for $f_G = f_P = 0$ and thickened symmetrically by a constant t using the software *Blender* to obtain sheet networks before cutting the specimens to cubes and exporting them as STL files. Detailed explanations of the design methods are found in [6].

2.2. Additive manufacturing

In accordance with Traub et al. [6], Tough 2000 is the base material used for stereolithography manufacturing of the test specimens. The printer used in the present study is a Formlabs Form 3L. The resin is cured selectively by a laser in a layer-by-layer fashion. According to the manufacturer [28], the SLA process offers the highest precision, resolution, and smoothest surface finishes among all additive manufacturing technologies. In association with the mechanical properties, a key advantage is the asserted isotropy [29]. During the printing process, monomers react to form covalent bonds within and between printed layers, promising isotropic material behavior. In the present study, six TPMS specimens are manufactured simultaneously using the default settings for Tough 2000. Thanks to the self-supporting feature of TPMS, cellular specimens are printed without internal support structures, while only free corners need additional support. Using a layer thickness of 0.05 mm printing 6 specimens with $RD = 0.1$ takes $27\,h$, with $RD = 0.7$ about $90\,h$.

After printing, the remaining liquid resin is removed by washing the specimens in isopropyl alcohol (IPA). According to Formlabs [30], specimens should be washed twice for ten minutes. It is observed that especially specimens with low sheet thicknesses t absorb IPA during the washing process and deform irregularly, as illustrated in Fig. 3(a). The main dimensions of Gyroid specimens with $RD = 0.1$ increase by about 11%. Thus, the washing cycles are reduced to one, and the remaining time in IPA is reduced to 5 to 10 min. Thin-walled specimens with $t < 0.7$ mm get damaged easily by soft touch and creep under their weight, whereas specimens of higher RD appear slightly bulbous after washing. The deformation reduces during drying under ventilation, but some concave curvature on the side that was in contact with the building plate (referred to as bottom) and convex deformation on the opposite side (top) remain. The influence of residual IPA on the degradation and embrittlement of the specimens was not investigated in this study. Post-curing is performed by rotating the specimens under a UV light source at 70 °C for one hour. The TPMS specimens are flattened by grinding on the top and bottom sides to meet the required parallelism tolerance specified in [22].

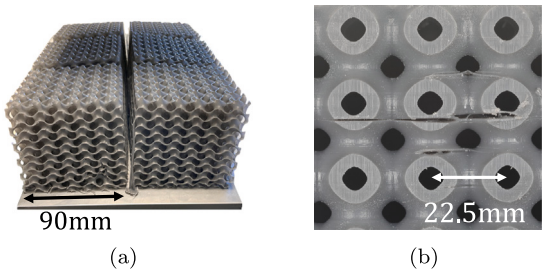

Fig. 3. Tough 2000 Gyroid specimens deformed due to absorption of IPA (a) and cracks in a Tough 2000 Primitive specimen after printing (b).

Further artifacts related to the manufacturing process SLA are observed with the Primitive specimens. The building plate is lifted between each printed layer, causing suction between the specimens and the resin tank and tensile stresses within the specimens. The tensile stresses during the printing process lead to deformed unit cells at $RD \leq 0.2$, gaps and cracks at $RD = 0.4$ (see Fig. 3(b)) and fracture of the specimens at $RD = 0.7$. Minor deformations and small cracks are deemed acceptable, but fractured specimens are excluded from testing.

The base material for additive manufacturing using selective laser sintering is Nylon 11. Specimens are produced on a Formlabs Fuse 1+ 30 W using the default settings for this base material and a layer height of 0.11 mm. The polymer–powder particles are sintered selectively to form a structure, while the printed part is embedded in loose powder. By nature, the process does not require support structures. Opposed to the SLA process with Tough 2000, final material properties are obtained without post-processing the printed part. Up to three TPMS specimens are manufactured in one run, requiring about $20\,h$ printing time. After completion of the printing process, loose powder adheres to the part's surface. It is removed using brushes and thin rods for the internal channels. The remaining powder is removed by sandblasting. This proves to be a good strategy for $n_{uc} = 4$ and $RD \leq 0.4$, but the poor accessibility of internal channels does not allow cleaning of specimens with $RD > 0.2$ for $n_{uc} > 4$, and the main dimensions specified above. Removed powder is mixed with fresh powder (in a 3:7 ratio) and is reused. The SLS printed specimens meet the parallelism tolerance and do not require further post-processing. Before testing, all specimens (Tough and Nylon) are conditioned in standard climate for $96\,h$.

The Figs. 4 and 5 summarize the manufacturability of both TPMS geometries and manufacturing techniques in a t over l_{uc} diagram using a traffic light system. In the diagram, green markers represent specimens that could be manufactured without difficulty, yellow markers represent specimens that could hardly be manufactured, and red markers represent specimens that could not be manufactured. In addition, manufacturable parameter sets are highlighted as regions. Isolines represent levels of constant RD. Table 1 contains the test matrix reduced to manufacturable specimens. Since this study focuses on application-related and industry-oriented findings, optimizing manufacturing parameters to expand the manufacturable regions is beyond its scope. Further information on improving the SLA process are found in [31,32]. An important distinction exists between specimens' manufacturability and their properties' validity. While some specimens made of Tough 2000 exhibit good manufacturability, they yield invalid data during compressive tests due to incompletely cured resin (see Section 3.1). Notably, all valid specimens contributing to the final model (Table 5) are exclusively based on $n_{uc} = 4$.

Table 1
Test matrix reduced to manufacturable series. Specimens represented by gray rows are not considered in the final model (Table 5).

geometry		main dim.	param. unit cell			rel. dens.	number	
		l, w, h mm	l_{uc} mm	t_f mm	n_{uc} -	RD_{design} -	SLA -	SLS -
G	RD_1	90	15.00	0.49	6	0.10	6	0
G	$\boldsymbol{RD_1}$	90	22.50	0.73	4	0.10	6	4
G	RD_2	90	15.00	0.98	6	0.20	6	2
G	$\boldsymbol{RD_2}$	90	22.50	1.46	4	0.20	6	2
G	RD_3	90	10.00	1.33	9	0.40	3	0
G	RD_3	90	15.00	1.99	6	0.40	6	0
G	$\boldsymbol{RD_3}$	90	22.50	2.98	4	0.40	5	2
G	RD_4	90	15.00	3.70	6	0.70	5	0
P	RD_1	90	15.00	0.64	6	0.10	0	2
P	$\boldsymbol{RD_1}$	90	22.50	0.96	4	0.10	3	2
P	$\boldsymbol{RD_2}$	90	22.50	1.93	4	0.20	3	2
P	RD_3	90	15.00	2.62	6	0.40	3	0
P	$\boldsymbol{RD_3}$	90	22.50	3.93	4	0.40	0	2
P	RD_4	90	10.00	3.28	9	0.70	3	0
M		⌀12.7; 50.8					6	6
S		⌀12.7; 25.4					6	6

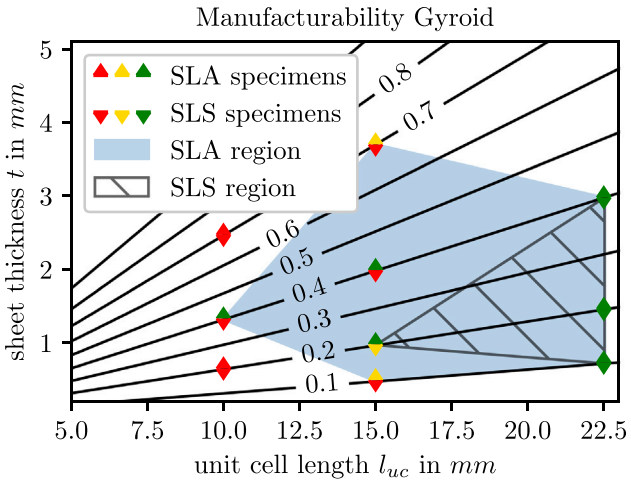

Fig. 4. Manufacturability of Tough 2000 (SLA) and Nylon 11 (SLS) Gyroid specimens. Contour lines indicate the relative density.

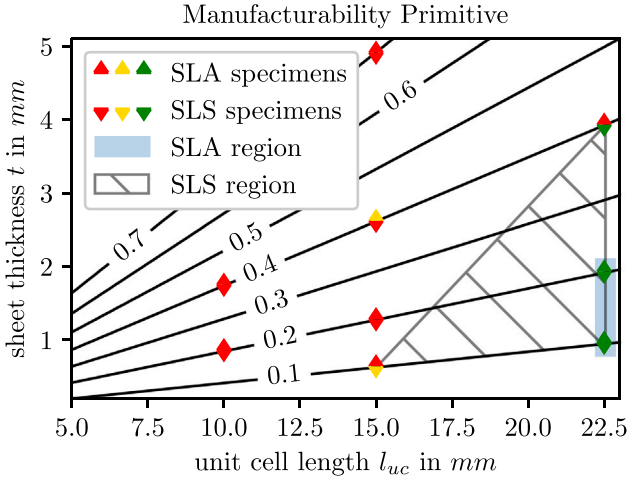

Fig. 5. Manufacturability of Tough 2000 (SLA) and Nylon 11 (SLS) Primitive specimens. Contour lines indicate the relative density.

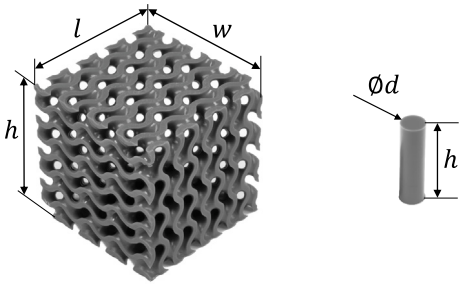

Fig. 6. Main dimensions l, w and $h = 90$ mm of an exemplary Gyroid specimen. Diameter $d = 12.7$ mm and height h of a solid specimen. h is parallel to the printing and loading direction.

2.3. Measuring the actual relative density of TPMS specimens

The actual relative density $RD = \rho^*/\rho_s$ of the TPMS specimens is determined based on the volume $V^* = l \cdot w \cdot h$ and the mass m^*. Specimen main dimensions l, w, and h, as shown in Fig. 6, are determined by averaging eight individual measurements for each dimension, using a digital caliper with automated data transfer and processing. The reference area for calculating stresses is $A_{ref} = l \cdot w$ and $A_{ref} = d^2 \cdot \pi/4$, respectively. The cellular solid's m^* is determined using a precision scale with a $0.1\,g$ resolution. To determine the density of the solid material ρ_s, six cuboids of each base material are manufactured using the same printing parameters. V and m are determined in like manner. For Gyroid specimens made of Tough 2000, the mean deviation between the actual relative density and the nominal value RD_{design} is less than 2.5%. Primitive specimens exhibit the greatest mean deviation (−5.8%) among Tough 2000 specimens due to the deformation mentioned above. All TPMS specimens made of Nylon 11 deviate by +2% up to +7% in average from RD_{design}. This suggests that loose powder remains even after sandblasting.

2.4. Experimental setup and testing

Two calibrated universal test machines equipped with compression platens are used for the compressive tests: A Zwick/Roell RetroLine 1476 with a 100 kN load cell for solid specimens and low relative density TPMS and a Zwick/Roell Z400E with a 400 kN load cell. The

cross-head movement is used as a measure of deformation and strain. Values are recorded in increments of $\Delta F = 1\ N$ or in time increments of $\Delta t = 0.1$ s, whatever occurs first. The compression platens are brought into contact to compensate for machine rigidity, and a calibration curve is recorded as the load increases.

Using a gauge, the specimens are placed in the center of the compression platen with the bottom side down. All specimens are loaded along their build direction. Initial load is not required according to the referenced standards but is helpful to prevent initial oscillations of the compressive stress–strain curves and to define a starting point. The cross-head is moved manually until $20\ N$ are applied. The compressive tests are conducted with constant velocity: for solid specimens 1.3 mm/min before and 5 mm/min after the yield point according to [21], 9 mm/min for TPMS according to [22,26]. The tests stop automatically when the maximum load is reached and manually in case of complete failure. No measurements are recorded during the return to the home position. During the tests, a camera records a series of images at a frame rate of 0.25/s to 0.5/s.

2.5. Determination of material properties

The compressive stress σ is calculated by dividing the compressive load F by the reference area A_{ref}. This stress is to be understood as an effective value. Non-uniform stress distributions on a cellular level, attributed to the geometry of the TPMS cell, are not considered during the tests. The same applies to the compressive strain $\varepsilon = |\Delta h|/h_0$ with h_0 representing the initial distance between the load platens. Both compressive stress and strain are defined to be positive. In the present study, the properties of TPMS specimens are denoted with an asterisk ($*$), following the nomenclature of Gibson and Ashby [11] for cellular solids, while the index s refers to the properties of the solid base material. The compressive moduli E^* and E_s are determined by the maximum slope of the initial increase in compressive stress. Linear regression is applied on subsequent strain intervals of $\Delta\varepsilon = 0.002$ (equal to the strain interval in [33]) to find the maximum slope of stress. To compensate for the initial toe in the stress–strain curve caused by settling effects, the zero crossing of the tangent at the maximum slope is defined as the new origin. All strain measurements refer to this origin. For the compressive strength σ^*_{max} and $\sigma_{max,s}$, the present study uses the definition specified in ASTM D1621 [22]. The compressive strength is defined as the stress at the yield point ($d\sigma/d\varepsilon = 0$) if this occurs at $\varepsilon \leq 0.1$. Otherwise, the compressive strength is the stress at $\varepsilon = 0.1$. This method is generally applicable and independent of local stress maxima. It aims at improved comparability between specimens of different relative densities and base materials. Let ε_y be the strain corresponding to the compressive strength. To prevent confusion, the terms *compressive yield strength* and *compressive maximum strength* are avoided in this study.

As none of the standards [22,26] covers parameters and characteristics related to the energy absorption of cellular structures, the approach by Li et al. [25] is implemented for the plateau stress σ^*_{plat} and energy absorption W^*. The energy absorption efficiency is:

$$\eta(\varepsilon) = \frac{1}{\sigma(\varepsilon)} \int_{\varepsilon_y}^{\varepsilon} \sigma(\varepsilon)\, d\varepsilon\,. \tag{6}$$

Its global maximum $d\eta(\varepsilon = \varepsilon_d)/d\varepsilon = 0$ determines a representative onset strain of densification ε_d. Fig. 7 illustrates a typical curve $\eta(\varepsilon)$ with a global maximum at $\varepsilon_d = 0.52$. The energy absorption is found by integration

$$W^* = \int_0^{\varepsilon_d} \sigma(\varepsilon)\, d\varepsilon \tag{7}$$

and the plateau stress is the average compressive stress in the plateau region

$$\sigma^*_{plat} = \frac{\int_{\varepsilon_y}^{\varepsilon_d} \sigma(\varepsilon)\, d\varepsilon}{\varepsilon_d - \varepsilon_y}\,. \tag{8}$$

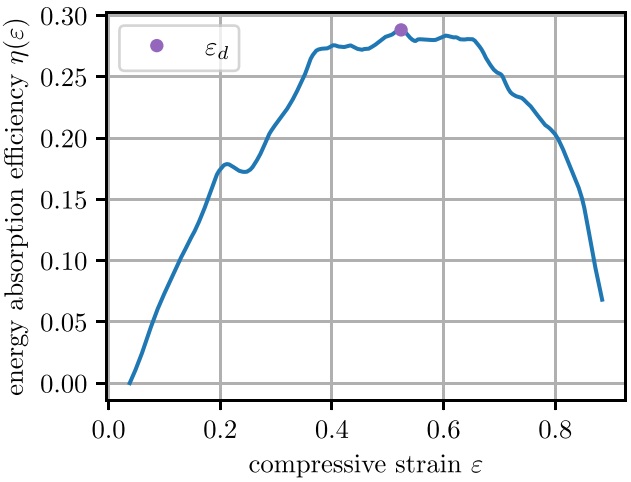

Fig. 7. Example curve for $\eta(\varepsilon)$. Determined for a Gyroid specimen, Tough 2000, $RD_1 = 0.1$ and $n_{uc} = 4$.

If a cellular specimen fails before the onset of densification is reached, both plateau stress and energy absorption cannot be calculated.

For each series of specimens with identical cellular parameters and base material, the mean properties and standard deviations are calculated.

2.6. Normalization

As mentioned above, normalizing the effective parameters E^*, σ^*_{max}, σ^*_{plat} and W^* pursues two objectives: the prediction of TPMS material parameters based on known base material properties and the investigation of the structural performance. To determine the performance of compressive modulus and strength, the relative parameters E^*/E_s and $\sigma^*_{max}/\sigma_{max,s}$ can be compared with the theoretical Voigt maximum. According to Schaedler et al. [34], the best possible scaling of the plateau stress is $\sigma^*_{plat} = \sigma_{max,s} \cdot RD$ assuming an ideal stress–strain response. Hence σ^*_{plat} is normalized with $\sigma_{max,s}$ as well. The maximum energy absorption W^*_{ideal} is achieved when $\sigma(\varepsilon) = \sigma^*_{plat} = \sigma_{max,s} \cdot RD$ and the onset of densification is delayed until porosities are compensated completely by compression. Assuming a Poisson's ratio of $\nu^* = 0$ this yields $\varepsilon_d = 1 - RD$ and $W^*_{ideal} = \sigma_{max,s} \cdot RD \cdot (1 - RD)$. In contrast to the other relative parameters, the relative energy absorption W^*/W^*_{ideal} is defined in an open interval $RD = (0, 1)$.

3. Experimental findings and interpretation

The quasi-static compression tests provide compressive stress–strain curves for solid and cellular specimens. Table 2 and 3 present the absolute mean values and standard deviations of cellular material properties for $n_{uc} = 4$. Relative material properties, such as the relative *modulus of elasticity*, *compressive strength*, *plateau stress*, and *energy absorption* are determined according to Section 2 considering the base material properties provided in Table 4.

In addition, images taken during the tests provide information on the specimens' deformation and failure. The results are presented through qualitative observations and quantitative analyses. Initially, the specimens' deformation and failure behavior are described and compared alongside the compressive stress–strain curves. The quantitative analysis involves averaged compressive stress–strain curves and a detailed examination of relative parameters modeled based on relative density.

Table 2
Absolute values (mean and standard deviation) for relative density RD, compressive modulus E^*, strength σ^*_{max} and strain ε_y corresponding to strength for multiple cellular series with $n_{uc} = 4$.

series	level	no.	RD	$E^*\,(MPa)$	$\sigma^*_{max}\,(MPa)$	ε_y
Tough, G	RD_1	6	0.100 ± 0.001	12.488 ± 1.947	0.245 ± 0.030	0.035 ± 0.001
	RD_2	6	0.197 ± 0.002	20.023 ± 1.874	0.461 ± 0.035	0.051 ± 0.004
	RD_3	5	0.401 ± 0.001	91.462 ± 7.809	3.069 ± 0.221	0.100 ± 0.000
Nylon, G	RD_1	4	0.102 ± 0.003	42.305 ± 4.766	1.065 ± 0.081	0.045 ± 0.001
	RD_2	2	0.215 ± 0.009	97.682 ± 0.089	3.350 ± 0.141	0.100 ± 0.000
	RD_3	2	0.412 ± 0.002	274.583 ± 3.273	9.769 ± 0.321	0.100 ± 0.000
Nylon, P	RD_1	2	0.107 ± 0.008	24.455 ± 2.115	0.832 ± 0.098	0.076 ± 0.001
	RD_2	2	0.207 ± 0.001	71.57 ± 3.204	2.602 ± 0.055	0.100 ± 0.000
	RD_3	2	0.412 ± 0.005	244.504 ± 1.370	9.074 ± 0.555	0.084 ± 0.023

Table 3
Absolute values (mean and standard deviation) for onset strain of densification ε_d, plateau stress σ^*_{plat} and volume specific energy absorption W^* for multiple cellular series with $n_{uc} = 4$.

series	level	ε_d	$\sigma^*_{plat}\,(MPa)$	$W^*\,(MPa)$
Tough, G	RD_1	0.517 ± 0.014	0.243 ± 0.019	0.123 ± 0.012
	RD_2	0.419 ± 0.010	0.560 ± 0.051	0.206 ± 0.019
	RD_3	0.509 ± 0.005	3.883 ± 0.244	1.828 ± 0.123
Nylon, G	RD_1	0.650 ± 0.023	0.999 ± 0.182	0.607 ± 0.134
	RD_2	0.635 ± 0.018	4.271 ± 0.133	2.284 ± 0.007
	RD_3	0.582	13.385	6.452

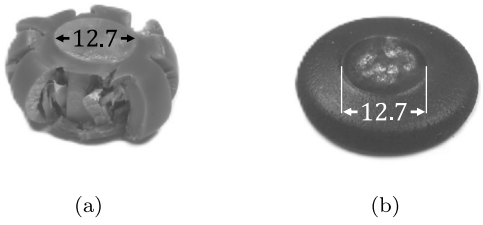

Fig. 9. Solid specimens of series "S" made of Tough 2000 (a) and Nylon 11 (b) after the compressive tests.

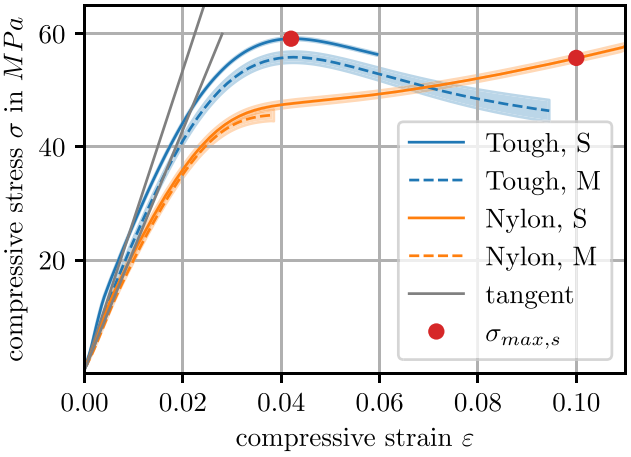

Fig. 8. Average compressive stress–strain curves for solid specimens.

3.1. Deformation and failure behavior

Fig. 8 illustrates the compressive stress–strain response of the solid specimens. Each graph shows a curve averaged over six specimens and a shaded region representing the standard deviation. According to ASTM D695 [21], the series "S" consists of shorter specimens to determine the compressive strength, whereas the compressive modulus is investigated using longer specimens with series "M".

Solid specimens made of Tough 2000 show a local maximum in stress. Series "S" specimens bulge as strain increases and eventually burst at $\varepsilon \approx 65\%$, as illustrated in Fig. 9(a). In contrast, solid specimens made of Nylon 11 exhibit a continuously increasing compressive stress and deform to a flat disk (Fig. 9(b)). Solid material properties for both base materials are provided in Table 4.

An exemplary compressive test of a Gyroid specimen made of Nylon 11 is illustrated in Figs. 10a–d. Before reaching the compressive strength, specimens deform uniformly. The following plateau regime is characterized by successive collapse of cell layers and undulations of the compressive stress. Gyroid structures made of Tough 2000 start to collapse in the center section of the specimen, whereas the corner cells initiate the collapse in the case of Primitive specimens. While the compression continues, collapsed layers densify, and the collapse proceeds towards neighboring cells until the entire structure densifies. As the collapse of individual cell layers progresses asynchronously, no clear relation between the observed deformation and oscillations in the stress–strain response can be found. Some Tough 2000 Primitive specimens deform and collapse regularly, and the number of oscillations matches the number of unit cells n_{uc}. It should be noted that the first layers densify well before the analytically determined onset of densification ε_d.

Material-dependent effects superimpose the general successive failure type of TPMS structures under compressive loads. Specimens of Tough 2000, especially for $RD \geq 0.4$, exhibit a deformation and failure behavior attributed to incompletely cured resin. The specimen's faces begin to bulge at low strain. Once the first cell layer densifies, the curvature radius at the bulging faces decreases, forming a distinct ridge. This ridge tears eventually, and viscous core material is squeezed outwards. Primitive specimens ($RD = 0.7$, $n_{uc} = 9$) exhibit cracks on the faces that grow and merge until whole faces are cut off the specimen. Fig. 11 illustrates such specimens after the compressive test: The core cells are destroyed and reduced to small debris particles. The resin inside the specimen is dense and sticky, giving evidence of inhomogeneous material properties. It is assumed that the compression tests, indicating incompletely cured base material, do not reveal the structural mechanical properties of the TPMS geometry. Thus, the structural properties obtained with Tough 2000 should be interpreted with reservation.

TPMS specimens made of Nylon 11 exhibit a different material-dependent behavior. While some specimens possess ductile behavior and deform and densify without any sign of brittle failure, others burst during the compressive test before the onset of densification ε_d is reached. All Primitive specimens made of Nylon 11 burst before the onset of densification, preventing the calculation of the energy absorption and plateau stress. Both failure types are observed for some Gyroid specimens of the same cellular parameters, suggesting irregularities in the manufacturing process. The Figs. 12a/b illustrate brittle failure of a Nylon 11 Gyroid and Primitive specimen. Both specimens fail after the ductile collapse and densification of neighboring cells.

Table 4
Properties of base materials Tough 2000 and Nylon 11. Manufacturer's information (M.i.) from [35,36].

parameter	ASTM	Tough 2000 (cured)	Nylon 11
tensile modulus (M.i.)	D638	2.2 GPa	1.6 GPa
compr. modulus E_s	D695	2.610 ± 0.108 GPa	2.135 ± 0.042 GPa
tensile strength (M.i.)	D638	46 MPa	49 MPa
compr. strength $\sigma_{max,s}$	D695	59.088 ± 0.240 MPa	55.44 ± 0.584 MPa
density ρ_s	–	$1.185 \pm 3.4\,e-3$ g/cm^3	$1.026 \pm 6.8\,e-3$ g/cm^3

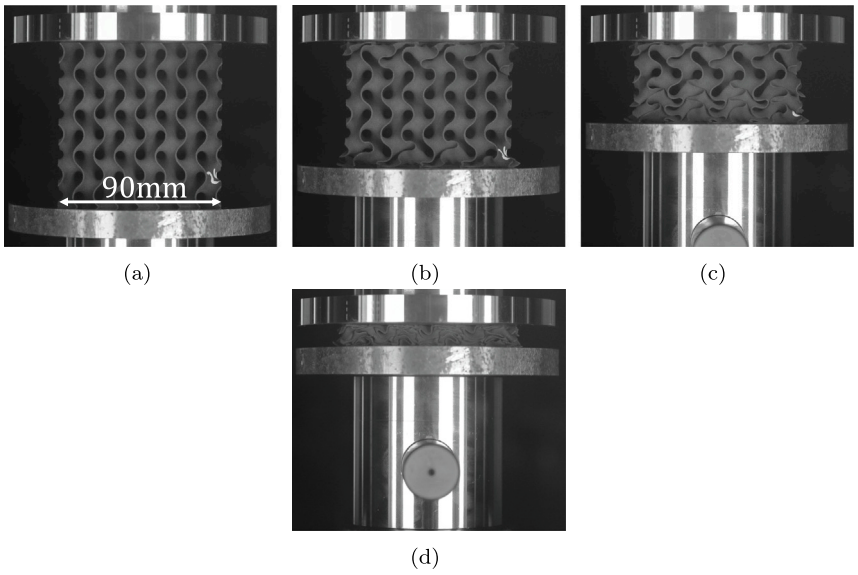

Fig. 10. Gyroid specimen (Nylon 11, $RD_2 = 0.1$, $n_{uc} = 4$) at $\varepsilon = 0$, 0.25, 0.5 and 0.85 compressive strain.

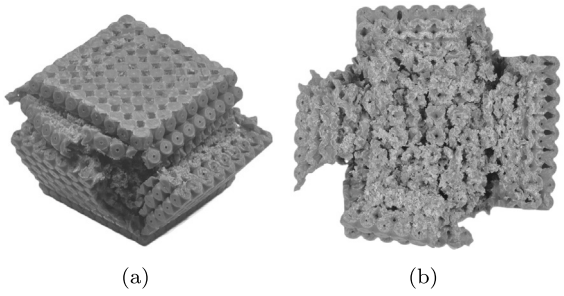

Fig. 11. Primitive specimens (Tough 2000, $RD = 0.7$, $n_{uc} = 9$) after compressive test.

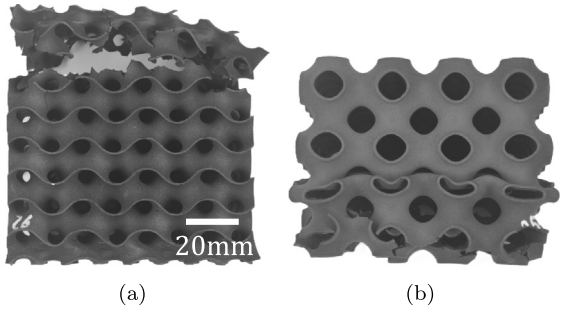

Fig. 12. Brittle failure of a Gyroid specimen (a) and a Primitive specimen (b), both $RD = 0,1$, $n_{uc} = 4$, after the ductile collapse and densification of neighboring cells.

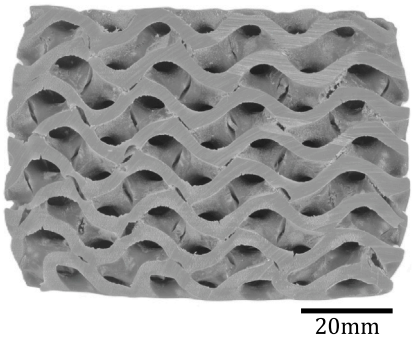

Fig. 13. Helix-shaped cracks inside a Gyroid specimen.

In a subsequent step, the fracture patterns of TPMS specimens that fail by successive collapse are investigated in detail after the compressive tests. Gyroid specimens exhibit cracks that differ in number and width depending on the base material and cellular parameters. However, the pattern itself is very similar for all Gyroid specimens tested. Fig. 13 shows a Tough 2000 Gyroid specimen cut in half. Cracks follow a helix-shaped course over multiple cell layers parallel to the loading direction. These findings agree well with the numerical investigations by Traub et al. [6] revealing highly stressed regions where the material is oriented along the load direction. It is concluded that the failure of Gyroid specimens under compressive load shows two characteristics: structural failure by successively collapsing cells and material failure on a cellular level in highly stressed regions.

Primitive specimens exhibit less pronounced cracks. Only a few are visible in the symmetry planes of cells made of Tough 2000.

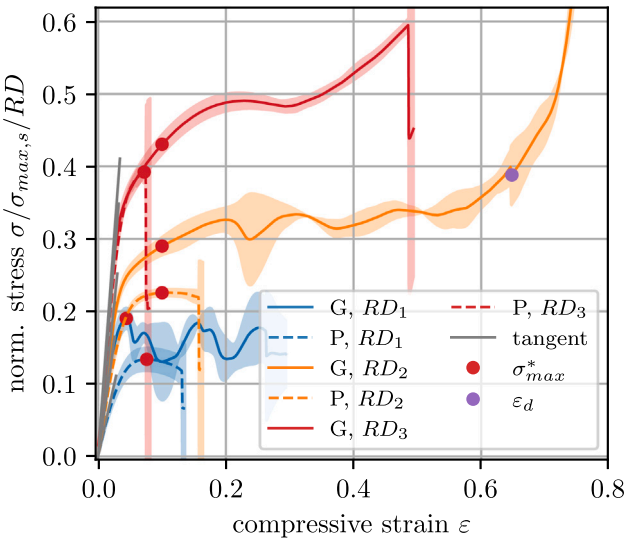

Fig. 14. Compressive stress–strain curves (average and standard deviation) of G and P specimens made of Nylon 11. $n_{uc} = 4 = const.$

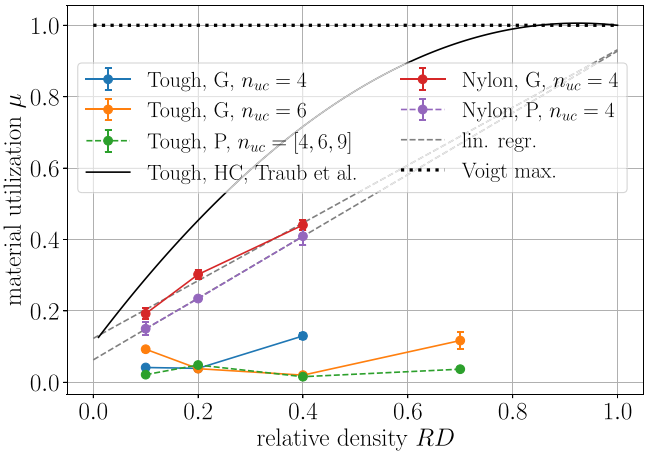

Fig. 15. Material utilization μ over RD of multiple series.

3.2. Reviewing the stress–strain curves

The comparability of compressive stress–strain curves requires normalizing the stress σ with the strength of the base material and the relative density. Here, the mean compressive strength $\sigma_{max,s}$ (Table 4) and the mean measured relative density RD (Table 2) are used. Fig. 14 illustrates normalized compressive stress–strain curves for TPMS specimens made of Nylon 11 by plotting the average normalized stress and the standard deviation (shaded region). The diagram marks the elastic straight lines, compressive strength, and the onset of densification. As the results obtained with specimens made of Tough 2000 are assumed to be not representative, the analysis focuses on the Nylon specimens.

Two stress–strain curves are averaged for each Nylon series, except the Gyroid series $n_{uc} = 4$, $RD_1 = 0.1$ that contains four specimens, constraining the statistical validity of the results. However, low scatter in the initial increase of compressive stress indicates a good repeatability of the elastic deformation. As soon as the first cells collapse in the plateau regime, scatter increases as the collapse and densification process differ for each cell and specimen.

Nylon TPMS specimens with $RD_1 = 0.1$ exhibit a local maximum stress below $\varepsilon = 0.1$, which defines the compressive strength σ^*_{max}. For specimens with higher relative densities, the criterion specified in ASTM D1621 [22] applies, and the compressive strength becomes the compressive stress at $\varepsilon = 0.1$. Primitive specimens with $RD_3 = 0.4$ constitute an exception, as premature fatal failure causes a stress maximum below $\varepsilon = 0.1$. The distinction between the strength definitions impacts the model of relative strength and has to be considered when comparing the mechanical models discussed in Section 3.4.

The normalized compressive stress–strain graphs are cut off at the lowest strain for fatal failure to occur. However, it may be concluded that the plateau regime of the Gyroid specimens tested in this study show a progressive trend for higher RD.

Normalizing the compressive strength σ^*_{max} with $\sigma_{max,s}$ and RD gives the material utilization μ. Fig. 15 shows the material utilization for both base materials, geometries, and all n_{uc} tested as a function of RD, providing mean values and error bars indicating the standard deviations. The Tough specimens tested have material utilization below 13%, with the lowest being 1.6%, attributed to the incompletely cured base material. In contrast, specimens made of Nylon, especially Primitive specimens, exhibit an approximately linear relation between the material utilization and the relative density, with the lowest being 13% (Primitive, $RD_1 = 0.1$) and the highest being 44% (Gyroid, $RD_3 = 0.4$). A linear curve fit yields the relations:

$$\mu_{G,Nylon} = 0.8085 \cdot RD + 0.1229 \quad (R^2 = 0.98468) \tag{9}$$

for the material utilization of Gyroid specimens and

$$\mu_{P,Nylon} = 0.8649 \cdot RD + 0.0628 \quad (R^2 = 0.99994) \tag{10}$$

for Primitive specimens.

These findings suggest that the fraction of material oriented along the compressive load increases with the relative density. For $RD \to 1$, a material utilization $\mu \to 1$ is to be expected. However, the linear curves in Fig. 15 predict a material utilization of ≈ 0.92. It is assumed that the accuracy of predicted material utilization values can be improved by testing specimens of higher relative density. For comparison, Fig. 15 additionally illustrates the material utilization of a honeycomb structure (HC) made of Tough 2000 as reported by Traub et al. [6]. In contrast to the linear curves for TPMS structures, it approximately asymptotically approaches $\mu \to 1$ for $RD \to 1$. At $RD_2 = 0.2$, the material utilization of the honeycomb structure outperforms the Primitive structures tested in this study by more than a factor of two. The Voigt maximum limit is not reached for $RD < 1$, even though all the material is oriented along the loading direction. This is because the onset of instability constrains compressive strength.

The onset of densification significantly impacts the plateau stress and energy absorption. This study determines the onset strain of densification ε_d with the energy absorption efficiency defined by Li et al. [25]. Fig. 16 illustrates the average ε_d and standard deviations for Nylon 11 Gyroid specimens. $\varepsilon_d\,(RD)$ can be described by a decreasing linear relation in good approximation:

$$\varepsilon_d = -0.2319 \cdot RD + 0.6764 \quad (R^2 = 0.98499) \tag{11}$$

For $RD \to 1$, the relation is not valid as $\varepsilon_d \to 0$ is expected for solid materials. However, for $RD \to 0$, the relation seems plausible. Increasing RD from 0.1 to 0.4 decreases ε_d by only $\Delta\varepsilon_d = 0.062$. This suggests that the onset strain of densification is not to be understood as a strain required to compensate for porosity $1 - RD$ by volume. The densification onset seems to be the strain required for new load paths to form within the collapsing sheet network, which stiffen the structure and ultimately maximize energy absorption efficiency. Primitive specimens are excluded from this investigation due to premature fatal failure.

3.3. Modeling compressive properties

The mechanical properties of the tested TPMS structures are modeled as a function of relative density using the Gibson-Ashby approach

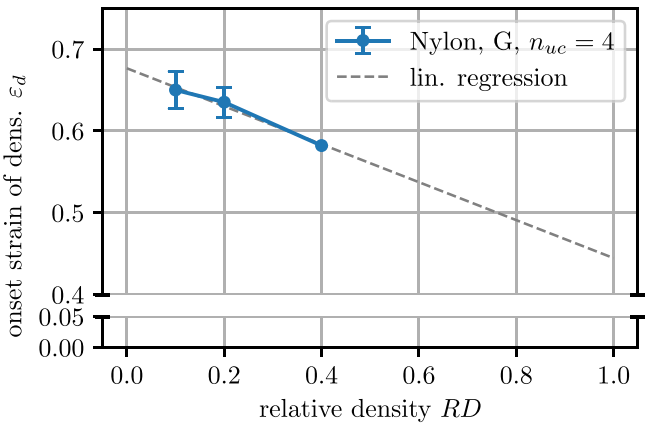

Fig. 16. Onset strain of densification for Gyroid specimens of Nylon 11.

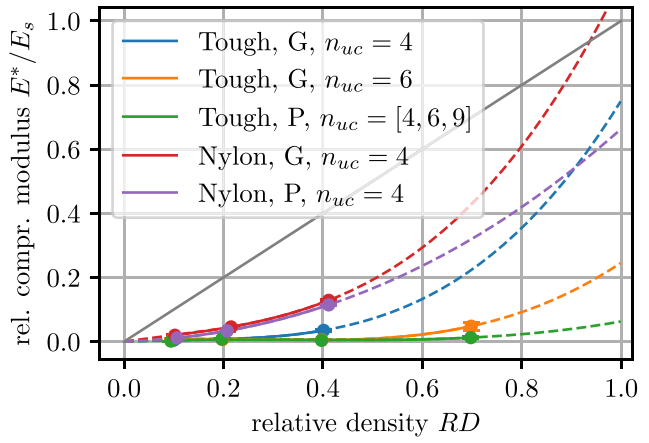

Fig. 17. E^*/E_s modeled using third order polynomial, without native (1; 1).

(eq. (1)). The best fit for the experimentally determined properties is found for $0 < \Phi < 1$ [6]. Although the Gibson–Ashby approach comprises scaling laws for the relative modulus of a cellular structure, Traub et al. [6] conclude that it also suffices for modeling the relative compressive strength. In the present study, Eq. (1) is modified and used to model all relative parameters P^*/P_s:

$$\frac{P^*}{P_s} = B \cdot RD + C \cdot RD^2 + D \cdot RD^3 . \tag{12}$$

Fig. 17 gives an overview of E^*/E_s as a function of RD for both geometries and base materials. The functions are extrapolated to cover the whole range of relative density. Error bars are barely visible, indicating a low scatter of the relative stiffness. The relative properties for $RD = 0$ and $RD = 1$ are inherent to cellular structures. While the Gibson-Ashby approach implicitly addresses $E^*/E_s(0) = 0$, the functions plotted in Fig. 17 do not account for $E^*/E_s(1) = 1$. Compared to the linear Voigt maximum limit, the TPMS structures' relative stiffnesses fall behind.

The results for specimens made of Tough stand out due to their exceptionally low relative moduli of $E^*/E_s < 0.1$ for all tested RD. It is found that the incompletely cured resin does not only lower stiffness and strength quantitatively but also affects the qualitative relation between structural properties and relative density: The relative parameters of Primitive and Gyroid structures with $n_{uc} > 4$ do not increase steadily with RD as local maxima are observed at $RD_2 = 0.2$. These results are excluded from the following discussion to omit data suspected of not being representative. Consequently, the influence of n_{uc} on the structural mechanics of the specimens cannot be investigated independently because it is dominated by manufacturing effects.

Table 5
Parameters to model relative properties according to eq. (12). Obtained using $n_{uc} = 4$ specimens, $RD = \{0.1, 0.2, 0.4\}$ including the native point (1, 1).

series	rel. property	parameters			R^2
		B	C	D	
Tough, G	E^*/E_s	0.1095	−0.6878	1.5784	0.99999
	$\sigma^*_{max}/\sigma_{max,s}$	0.0578	−0.3344	1.2766	0.99999
	$\sigma^*_{plat}/\sigma_{max,s}$	0.0297	−0.0946	1.0649	0.99999
	W^*/W^*_{ideal}	0.0588	0.4366	0.5046	0.99961
Nylon, G	E^*/E_s	0.184	−0.0417	0.8577	0.99999
	$\sigma^*_{max}/\sigma_{max,s}$	0.1326	0.6154	0.2520	0.99999
	$\sigma^*_{plat}/\sigma_{max,s}$	0.0538	1.2720	−0.3258	0.99999
	W^*/W^*_{ideal}	1,0944	0.3577	−0.4521	0.99993
Nylon, P	E^*/E_s	0.0985	0.1145	0.7871	0.99999
	$\sigma^*_{max}/\sigma_{max,s}$	0.0661	0.7166	0.7871	0.99999

Nylon specimens tested in this study outperform the Tough specimens of the same RD by a factor of at least three in relative modulus. Gyroid and Primitive specimens differ marginally, with the Gyroid exhibiting slightly higher relative moduli.

3.4. Assessment of the mechanical models

To verify the relative properties obtained, the native point (1; 1) is added to the curve fit, and the models for the Nylon and Tough series (both $n_{uc} = 4$) are compared to numerical and experimental results of Traub et al. [6]. All parameters of the modeled relative cellular properties can be found in Table 5. Fig. 18 contrasts the models for $E^*/E_s(RD)$. Compared to tested Gyroid specimens made of Nylon 11, the mechanical model obtained using FEA yields higher relative moduli by 30 to 50%. This is explained by the idealization of experimental conditions in the FE simulation: A perfectly shaped Gyroid cell in an infinite compound is simulated. The linear elastic base material is free of manufacturing imperfections, and the load is applied homogeneously. Consequently, the FE analysis can be regarded as a practical upper limit for the experimentally tested Gyroid cell.

Even though Traub et al. also use Tough 2000 as the base material for their experimental results, the measured relative stiffnesses of Tough 2000 Gyroid specimens ($n_{uc} = 4$) in the present study is lower by a factor of 3 at $RD_2 = 0.2$ and by a factor of ≈ 2.2 at $RD_3 = 0.4$. Traub et al. do not report noticeable constraints concerning the curing of the base material. Still, the Gyroid model for Nylon 11 exhibits higher relative stiffness than Traub's Tough model, exceeding it by a factor of 2 at $RD_2 = 0.2$ and by a factor of 1.25 at $RD_3 = 0.4$. Furthermore, the relative stiffness of the Gyroid structure is slightly higher than the relative stiffness of the Primitive in the Nylon model, contradicting the experimental results by Traub et al. This suggests that the experimental results by Traub et al. though visually not noticeable during the tests, were also affected by incompletely cured Tough 2000. In an additional experimental series concerning the homogeneity of cured Tough 2000, it is shown that the core material of thin plates with a thickness ≥ 2 mm does not cure completely when manufactured following the process mentioned above.

In the style of Fig. 18, Fig. 19 shows the relative compressive strength $\sigma^*_{max}/\sigma_{max,s}(RD)$. In FEA, Traub et al. [6] define the compressive strength as the minimum effective stress on the TPMS structure that results in localized concentrations of von Mises stress, exceeding the strength of the base material. Visually and in accordance with [6], the models appear to be very similar to $E^*/E_s(RD)$. For $RD_1 = 0.1$, the Gyroid's FE model predicts a 34% higher relative strength than the experimentally determined Nylon model. Interestingly, the measured relative strength of the Gyroid specimens made of Nylon equals or exceeds the FE results for $RD \geq 0.2$. The definitions of σ^*_{max} are found to contribute to this: In the experiments for $RD_1 = 0.1$, the criterion is based on the presence of a local maximum in the compressive stress–strain curve, whereas for $RD \geq 0.2$, the criterion for the absence of a

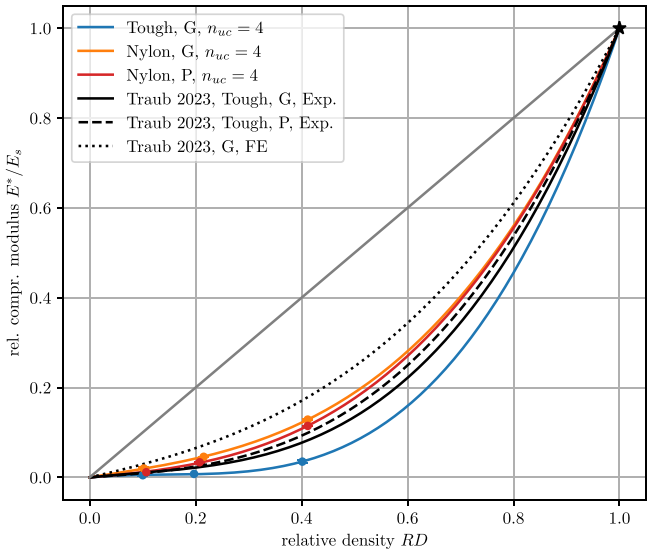

Fig. 18. Relative compressive moduli determined in this study and by Traub et al. [6] including the native point (1, 1).

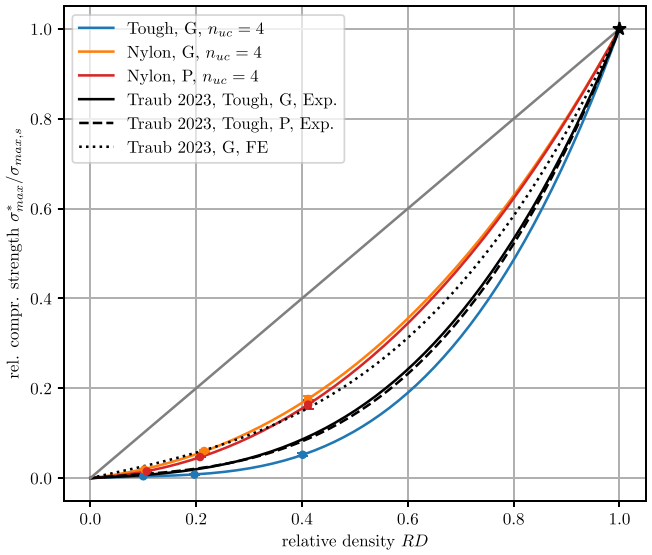

Fig. 19. Relative compressive strength determined in this study and by Traub et al. [6] including the native point (1, 1).

local maximum ($\sigma^*_{max} = \sigma(\varepsilon = 0.1)$) is applied. This criterion overestimates the actual compressive strength compared to the criterion based on a local stress maximum. The findings suggest that both criteria for the compressive strength are inconsistent and indicate further research needs.

Based on the comparison between the modeled relative properties for specimens made of Tough 2000 and Nylon 11, it is concluded that both material-independent formulations cannot validate each other. Major influences related to the manufacturing invalidate the normalization P^*/P_s of Tough 2000. Consequently, previously published models for Gyroid and Primitive sheet networks are compared to verify the results. Only references that provide information on the base material properties, such as Abou-Ali et al. [16] (PA 1102) and Zhang et al. [9] (stainless steel) come into consideration. The base material properties they provide may not accurately reflect the properties of additively manufactured solid parts tested under the same conditions as their cellular specimens, so the models should be interpreted with caution.

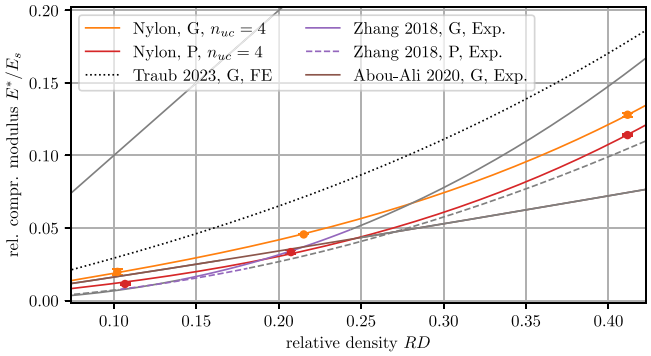

Fig. 20. Comparison of the relative compressive moduli and results from literature [6,9,16].

These studies investigate relative density intervals from 0.1 up to 0.525 and do not consider the native point (1; 1). Thus, the comparison between the studies is limited to this range of relative densities.

Fig. 20 plots the relative modulus models for Nylon specimens found in the present study and contrasts the results with the power laws from [9,16] and the Gibson–Ashby model from Traub et al. [6]. Curves representing the power laws are each colored in the investigated RD range. The function for the Gyroid geometry found by Abou-Ali et al. (base material PA 1102) agrees remarkably well with the present study at low relative densities but exhibits a lower slope. At $RD \approx 0.24$, it intersects with the Nylon P model.

In contrast to Abou-Ali et al. [16], the model for the Gyroid geometry found by Zhang et al. [9] (base material stainless steel) starts at a lower relative stiffness at $RD \approx 0.1$ and shows a steeper increase. At $RD = 0.24$, the relative stiffness for the Gyroid structure predicted by Zhang et al. is 10% below the Nylon G model. The best agreement among the compared studies is observed for the Primitive model by Zhang et al. and the present study. Their curves are parallel in good approximation even beyond the highest relative density investigated by Zhang et al. At $RD = 0.25$, both models differ by 8%.

The findings for the relative modulus support the initial hypothesis of the present study, to model cellular material properties using relative parameters and validate this material-independent approach by comparing multiple models. A good agreement is observed for the selective relative density $RD_1 = 0.1$ between the results of the present study and those of Abou-Ali et al. for the Gyroid, based on the precisely defined relative compressive modulus. Comparing the power-law approach with the Gibson–Ashby model is more challenging due to differing considerations regarding the native point (1; 1). Nevertheless, the strong agreement between the Nylon P and Zhang P models highlights that the material-invariant approach effectively enables the comparison of TPMS structures across different base material classes.

4. Discussion

Compressive tests of high relative density Tough 2000 specimens reveal inhomogeneous material properties and the presence of viscous resin within the specimens. These findings suggest that, for TPMS specimens made of Tough 2000, the cellular parameters and primary dimensions are the most significant factors influencing their mechanical properties. In contrast to the suggestion in [6], specimens larger than $40 \times 40 \times 40$ mm^3 are not found to decrease the influence of manufacturing imperfections. The specimens swell and deform irregularly at low relative densities, requiring further post-processing before testing, while high relative densities prevent effective curing and even cause decreasing relative properties. This also constrains the validity of the normalization P^*/P_s and, thus, the significance of the structural performance. Eventually, the mechanical properties of Tough 2000 specimens are considered not representative in this study.

As Tough specimens with lower n_{uc} perform better, larger unit cells and internal channels are assumed to improve the curing process. For TPMS specimens made of Nylon 11, the limited accessibility to internal channels significantly constrains the manufacturability of specimens with $n_{uc} > 4$ and the main dimensions used in the present study. Hence, no conclusion can be drawn on how many unit cells are required to approximate an infinite compound. The results suggest that Tough 2000 should be avoided as a base material for mechanically loaded TPMS structures. For future studies, other types of resin that do not require extensive post-curing are suggested. Additionally, alternative manufacturing approaches, such as the thermal solvent extraction based AM technique proposed by Sharma et al. [37] can be considered.

More reliable data on the structural–mechanical properties of TPMS specimens are gathered using Nylon 11 as a base material. Comparing the different material-independent models with the results from Traub et al. [6], a trend is observed: The fewer defects related to the manufacturing of the TPMS specimens, the less the experimentally obtained results differ from the FE model.

In that regard, the problem of standardized, consistent definitions for experimentally measured compressive strength arises: Depending on the criterion applied, the measured relative compressive strength is below, equals, or exceeds the numerical results with increasing relative density. The numerical results, however, serve as a practical upper limit, as the relative strength at $RD_1 = 0.1$ and the precisely defined relative moduli confirm. Thus, the modeled relative strength for Nylon 11 is expected to be below the Traub FE model for $0 < RD < 1$. The 10%-strain criterion overestimates the actual compressive strength for $RD_2 = 0.2$ and $RD_3 = 0.4$, yielding inconsistent values for the compressive strength as a function of RD. Consequently, the 10%-strain criterion is not applicable for medium relative densities. Furthermore, for high relative densities and the condition of an onset strain of densification ε_d below 10%, the 10%-strain criterion is also not applicable. Motivated by incomparable strength definitions in the literature, the present study uses standardized methods aiming at consistent results. The findings, however, reveal major drawbacks of the existing criteria. This study's results suggest defining a continuous strength criterion that reflects the relative density over the complete range $0 < RD < 1$ and does not rely solely on local stress maxima.

This study does not pursue its initial approach of defining a material-independent model using Tough 2000 specimens and validating it using the Nylon specimens because manufacturing effects dominate the properties of Tough specimens. Alternatively, literature results are used to assess the material-independent character of the model obtained for the base material Nylon 11. Good agreement regarding the relative modulus is observed between this and other studies [6,9,16]. Thus, the material-invariant character of the relative modulus is considered validated. Given a stable, predictable manufacturing method, TPMS structures can be engineered concerning stiffness based on known base material properties and the model for the relative modulus presented in this study (Table 5). The material-invariant compressive strength could not be validated in this study. A novel strength criterion is expected to validate material-independent strength modeling. Nonetheless, the modeled relative strength can be used in preliminary design with a higher margin of safety. The validity of the modeled relative energy absorption is constrained by the brittle failure of some Nylon 11 specimens. Therefore, the results of this study alone do not allow for a conclusive design of the leading-edge suction panels in terms of energy absorption. A distinction between ductile and brittle failure types within the material-independent approach is proposed to allow for representative plateau stress and energy absorption.

5. Conclusion

The present study aims to characterize the mechanical properties of TPMS structures using material-invariant models and relative parameters. Gyroid and Primitive specimens are manufactured as sheet networks from Tough 2000 resin and Nylon 11 powder and investigated experimentally under quasi-static compressive loads. Effective material properties are derived from the resulting compressive stress–strain curves, averaged, and fitted as a function of the relative density.

An increasing linear relation describes the material utilization of Nylon 11 TPMS specimens in good approximation. The maximum material utilization measured in the present study is 44% for a Gyroid structure at $RD = 0.4$. Both Gyroid and Primitive structures exhibit very similar relative stiffnesses and strengths, with the Gyroid performing slightly better than the Primitive. Compared to Traub et al. [6], it is concluded that the experimentally determined mechanical models approach the practical upper limit provided by numerical simulations due to fewer constraining influences related to manufacturing. However, brittle failure of all Nylon P and some Nylon G specimens before the onset of densification limits the plateau stress and energy absorption determination.

The mechanical behavior of Tough specimens is dominated by manufacturing variant effects and related to incompletely cured resin, causing values of material utilization as low as 2 % to 13 %. The relative strength and stiffness are below 0.1 for $0.1 \leq RD \leq 0.7$ for all tested Tough specimens. For $n_{uc} > 4$, the relative properties do not increase steadily with RD. Consequently, the Tough specimens tested in the present study do not enable representative material-invariant models and cannot validate the model based on Nylon specimens. Instead, literature results, though not representative without limitation, are used for comparison. Comparable relative stiffnesses are obtained using different base material classes. Thus, the material-invariant approach based on relative moduli is supported by the present study and work of other research groups [6,9,16] within their investigated interval of relative densities. Further studies to conclusively validate the results on a generalized level exploit the potential of this approach.

The authors propose future studies to validate the material-invariant model further. Inconsistent definitions of mechanical properties are partly the reason for the lack of comparability between studies of different research groups. The present work shows that the consistent use of definitions is challenging, even within a single study. A criterion yielding consistent strength for all relative densities independent of local stress maxima must be defined. A second, comparable study is encouraged to confirm the material-invariant model described in this study using a different base material and manufacturing method that does not require extensive post-processing and ensures successive collapse of the TPMS structure. Building on the initial goal of designing multifunctional suction panels, future studies will extend the investigations to higher strain rates through drop-weight tests. The results of this study provide a foundation for accurately dimensioning the core structure. With current advances in additive manufacturing, identifying a base material that meets the required stiffness, strength, and ductility will enable the production of suction panels ready for practical applications, moving beyond mere demonstration purposes.

CRediT authorship contribution statement

Henri Kammler: Writing – review & editing, Writing – original draft, Visualization, Validation, Software, Methodology, Investigation, Formal analysis, Data curation, Conceptualization. **Jan Kube:** Writing – review & editing, Writing – original draft, Visualization, Validation, Supervision, Project administration, Methodology, Investigation. **Hendrik Traub:** Writing – review & editing, Writing – original draft, Visualization, Validation, Supervision, Software, Project administration, Methodology, Investigation, Funding acquisition, Conceptualization. **Christian Hühne:** Writing – review & editing, Supervision, Resources, Project administration, Funding acquisition.

Declaration of Generative AI and AI-assisted technologies in the writing process

During the preparation of this work, the authors used ChatGPT to suggest improvements in language and readability. After using this tool, the authors reviewed and edited the content as needed and take full responsibility for the publication's content.

Declaration of competing interest

The authors declare that they have no known competing financial interests or personal relationships that could have appeared to influence the work reported in this paper.

Acknowledgments

This research was funded by the Deutsche Forschungsgemeinschaft (DFG, German Research Foundation), Germany under Germany's Excellence Strategy – EXC 2163/1-Sustainable and Energy Efficient Aviation – Project-ID 390881007 and by the German Federal Ministry for Economic Affairs and Climate Action (BMWK) under project number 20A2103D (MuStHaF).

Data availability

Data will be made available on request.

References

[1] N. Beck, T. Landa, A. Seitz, L. Boermans, Y. Liu, R. Radespiel, Drag Reduction by Laminar Flow Control, Energies 11 (1) (2018) 252, http://dx.doi.org/10.3390/en11010252.

[2] K. Krishnan, O. Bertram, O. Seibel, Review of hybrid laminar flow control systems, Prog. Aerosp. Sci. 93 (2017) 24–52, http://dx.doi.org/10.1016/j.paerosci.2017.05.005.

[3] H. Traub, J. Wolff, S. Jose, L. Lobitz, M. Schollerer, C. Hühne, Concept and design of extended hybrid laminar flow control suction panels, Sci. Rep. (2021) http://dx.doi.org/10.21203/rs.3.rs-924184/v1.

[4] H. Traub, J. Kube, S. Jose, A. Prasannakumar, C. Hühne, Structural and aerodynamic characteristics of micro-perforated porous sheets for laminar flow control, in: ASME 2024 Aerospace Structures, Structural Dynamics, and Materials Conference, American Society of Mechanical Engineers, 2024, p. 10, http://dx.doi.org/10.1115/SSDM2024-121620.

[5] L. Lobitz, H. Traub, M. Overbeck, M. Bień, S. Heimbs, C. Hühne, J. Friedrichs, P. Horst, Aircraft wing design for extended hybrid laminar flow control, Aerospace 10 (11) (2023) 938, http://dx.doi.org/10.3390/aerospace10110938.

[6] H. Traub, M. Sprengholz, D. Teufel, C. Hühne, Structural-mechanical characterisation of triply periodic minimal surface sheet networks: simulation and experiment, in: AIAA SCITECH 2023 Forum, American Institute of Aeronautics and Astronautics, Reston, Virginia, 2023, http://dx.doi.org/10.2514/6.2023-2076.

[7] O. Al-Ketan, R.K.A. Al-Rub, Multifunctional mechanical metamaterials based on triply periodic minimal surface lattices, Adv. Eng. Mater. 21 (10) (2019) 1900524, http://dx.doi.org/10.1002/adem.201900524.

[8] F.S.L. Bobbert, K. Lietaert, A.A. Eftekhari, B. Pouran, S.M. Ahmadi, H. Weinans, A.A. Zadpoor, Additively manufactured metallic porous biomaterials based on minimal surfaces: A unique combination of topological, mechanical, and mass transport properties, Acta Biomater. 53 (2017) 572–584, http://dx.doi.org/10.1016/j.actbio.2017.02.024.

[9] L. Zhang, S. Feih, S. Daynes, S. Chang, M.Y. Wang, J. Wei, W.F. Lu, Energy absorption characteristics of metallic triply periodic minimal surface sheet structures under compressive loading, Addit. Manuf. 23 (2018) 505–515, http://dx.doi.org/10.1016/j.addma.2018.08.007.

[10] M.F. Ashby, The properties of foams and lattices, Philos. Trans. Ser. A, Math. Phys. Eng. Sci. 364 (1838) (2006) 15–30, http://dx.doi.org/10.1098/rsta.2005.1678.

[11] L.J. Gibson, M.F. Ashby, Cellular solids: Structure and properties, second ed., in: Cambridge solid state science series, Cambridge Univ. Press, Cambridge, 1997.

[12] J. Bauer, L.R. Meza, T.A. Schaedler, R. Schwaiger, X. Zheng, L. Valdevit, Nanolattices: An emerging class of mechanical metamaterials, Adv. Mater. 29 (40) (2017) 1701850, http://dx.doi.org/10.1002/adma.201701850.

[13] E. Lord, A. Mackay, Periodic minimal surfaces of cubic symmetry, Current Sci. 85 (2003) 346–362.

[14] D.W. Abueidda, M. Bakir, R.K. Abu Al-Rub, J.S. Bergström, N.A. Sobh, I. Jasiuk, Mechanical properties of 3D printed polymeric cellular materials with triply periodic minimal surface architectures, Mater. Des. 122 (2017) 255–267, http://dx.doi.org/10.1016/j.matdes.2017.03.018.

[15] O. Al-Ketan, R. Rowshan, R.K. Abu Al-Rub, Topology-mechanical property relationship of 3D printed strut, skeletal, and sheet based periodic metallic cellular materials, Addit. Manuf. 19 (2018) 167–183, http://dx.doi.org/10.1016/j.addma.2017.12.006.

[16] A.M. Abou-Ali, O. Al-Ketan, D.-W. Lee, R. Rowshan, R.K. Abu Al-Rub, Mechanical behavior of polymeric selective laser sintered ligament and sheet based lattices of triply periodic minimal surface architectures, Mater. Des. 196 (2020) 109100, http://dx.doi.org/10.1016/j.matdes.2020.109100.

[17] M.M. Bazyar, S.B. Tabary, D. Rahmatabdi, K. Mohammadi, R. Hashemi, A novel practical method for the production of functionally graded materials by varying exposure time via photo-curing 3D printing, J. Manuf. Process. 103 (2023) 136–143, http://dx.doi.org/10.1016/j.jmapro.2023.08.018, URL https://www.sciencedirect.com/science/article/pii/S1526612523007958.

[18] Z. Luo, Q. Tang, Q. Feng, S. Ma, J. Song, R. Setchi, F. Guo, Y. Zhang, Finite element analysis of the mechanical properties of sheet- and skeleton-gyroid Ti6Al4V structures produced by laser powder bed fusion, Thin-Walled Struct. 192 (2023) 111098, http://dx.doi.org/10.1016/j.tws.2023.111098.

[19] M. Jin, Q. Feng, X. Fan, Z. Luo, Q. Tang, J. Song, S. Ma, Y. Nie, P. Jin, M. Zhao, Investigation on the mechanical properties of TPMS porous structures fabricated by laser powder bed fusion, J. Manuf. Process. 76 (2022) 559–574, http://dx.doi.org/10.1016/j.jmapro.2022.02.035.

[20] W. Song, K. Mu, G. Feng, Z. Huang, Y. Liu, X. Huang, L. Xiao, Mechanical properties of 3D printed interpenetrating phase composites with TPMS architectures, Thin-Walled Struct. 193 (2023) 111210, http://dx.doi.org/10.1016/j.tws.2023.111210.

[21] ASTM D20 Committee, Standard Test Method for Compressive Properties of Rigid Plastics D695-15, fifteenth ed., (D695) ASTM International, West Conshohocken, PA, 2015, http://dx.doi.org/10.1520/D0695-15.

[22] ASTM D20 Committee, Standard Test Method for Compressive Properties of Rigid Cellular Plastics D1621-16, sixteenth ed., (D1621) ASTM International, 2016, http://dx.doi.org/10.1520/D1621-16.

[23] A.M. Abou-Ali, O. Al-Ketan, R. Rowshan, R. Abu Al-Rub, Mechanical response of 3D printed bending-dominated ligament-based triply periodic cellular polymeric solids, J. Mater. Eng. Perform. 28 (4) (2019) 2316–2326, http://dx.doi.org/10.1007/s11665-019-03982-8.

[24] D.W. Abueidda, M. Elhebeary, C.-S. Shiang, S. Pang, R.K. Abu Al-Rub, I.M. Jasiuk, Mechanical properties of 3D printed polymeric gyroid cellular structures: Experimental and finite element study, Mater. Des. 165 (2019) 107597, http://dx.doi.org/10.1016/j.matdes.2019.107597.

[25] Q.M. Li, I. Magkiriadis, J.J. Harrigan, Compressive strain at the onset of densification of cellular solids, J. Cell. Plast. 42 (5) (2006) 371–392, http://dx.doi.org/10.1177/0021955X06063519.

[26] DIN Deutsches Institut für Normung e V, Harte Schaumstoffe – Bestimmung der Druckeigenschaften (ISO 844:2021), two thousand and twenty first ed., (844) Berlin, DE, 2021.

[27] H.G. von Schnering, R. Nesper, Nodal surfaces of Fourier series: Fundamental invariants of structured matter, Z. Für Phys. B Condens. Matter 83 (3) (1991) 407–412, http://dx.doi.org/10.1007/BF01313411.

[28] Formlabs, Stereolithografie (SLA) 3D-druck: Der ultimative leitfaden, 2024, URL https://formlabs.com/de/blog/leitfaden-stereolithografie-sla-3d-druck/.

[29] Formlabs, Validating isotropy in SLA 3D printing, 2024, URL https://formlabs.com/blog/isotropy-in-SLA-3D-printing/.

[30] Formlabs Customer Support, Verwendung von Tough 2000 Resin, 2023, URL https://support.formlabs.com/s/article/Using-Tough-Resin?language=de.

[31] M.P. Watters, M.L. Bernhardt, Curing parameters to improve the mechanical properties of stereolithographic printed specimens, Rapid Prototyp. J. 24 (1) (2018) 46–51, http://dx.doi.org/10.1108/RPJ-11-2016-0180.

[32] M. Forstmeier, J. LeBlanc, E. Warner, K. Merlo, Quantification of the effects of print parameters on the mechanical performance of low force stereolithography parts, Int. J. Light. Mater. Manuf. 7 (6) (2024) 958–967, http://dx.doi.org/10.1016/j.ijlmm.2024.05.012.

[33] DIN EN ISO 604:2003-12, Kunststoffe - Bestimmung von Druckeigenschaften (ISO 604:2002): Norm, DIN Deutsches Institut für Normung e. V, Berlin, DE, 2003.

[34] T.A. Schaedler, C.J. Ro, A.E. Sorensen, Z. Eckel, S.S. Yang, W.B. Carter, A.J. Jacobsen, Designing metallic microlattices for energy absorber applications, Adv. Eng. Mater. 16 (3) (2014) 276–283, http://dx.doi.org/10.1002/adem.201300206.

[35] Formlabs, Datenblatt Tough 2000 Resin, first ed., 2020, URL https://formlabs.com/de/materials/tough-durable/.

[36] Formlabs, Datenblatt Nylon 11 Powder, 02 ed., 2024, URL https://formlabs.com/de/materials/sls-powders/#nylon-11.

[37] P. Sharma, C. Das, P. Sreeramagiri, G. Balasubramanian, Additively manufactured lightweight and hard high-entropy alloys by thermally activated solvent extraction, High Entropy Alloy. Mater. 2 (1) (2024) 41–47, http://dx.doi.org/10.1007/s44210-024-00029-z, URL https://link.springer.com/article/10.1007/s44210-024-00029-z.